machines

MDPI

Article

Influence-Matrix-Accelerated Resistor-Network-Based Temperature Field Reconstruction for PCB Reflow Soldering

Árpád Gábor Móré [1,*], Ádám Móré [1,2], Rafael Ruben Boros [2,3] and Attila Trohák [1]

[1] Faculty of Mechanical Engineering and Informatics, Institute of Automation and Info-Communication, University of Miskolc, 3515 Miskolc, Hungary; adam.more@uni-miskolc.hu (Á.M.); attila.trohak@uni-miskolc.hu (A.T.)
[2] Institute of Engineering and Agricultural Sciences, University of Nyíregyháza, 4400 Nyíregyháza, Hungary; boros.ruben@nye.hu
[3] Institute of Physics and Electrical Engineering, University of Miskolc, 3515 Miskolc, Hungary
* Correspondence: arpad.more@uni-miskolc.hu

Abstract

During reflow soldering, the spatial temperature distribution over a printed circuit board cannot be determined directly from a small number of measurement points; therefore, a reconstruction method is required. This study investigates a resistor-network reconstruction method based on the discrete Laplace equation and its acceleration using an influence matrix. The input data comprised seven K-type thermocouple readings at one selected instant from a single PCB (approximately 10 × 15 cm), represented by a 10 × 15 cell grid. The baseline method reconstructed the complete field using Jacobi iteration, whereas the accelerated method used a linear combination of precomputed unit-excitation basis fields. Validation included sensor-wise leave-one-out tests at internal measurement points, comparison with inverse distance weighting, and tests on rectangular and concave domains. For the available measurement state, the resistor-network method achieved a mean absolute validation error of 1.39 °C, while the online influence-matrix evaluation was approximately 54 times faster than the baseline method. The results indicate that, for fixed geometry and sensor layout, the method may support fast, repeated spatial reconstruction.

Keywords: PCB; reflow soldering; temperature field reconstruction; resistor network; influence matrix; discrete Laplace equation

1. Introduction

Reflow soldering is a key thermal process in electronics assembly. Soldering quality is governed not only by the set oven-zone temperatures and conveyor speed, but also by the combined effects of the printed circuit board (PCB), the components, and local heat-transfer conditions. Consequently, different points on the board may have different temperatures at the same instant, whereas process evaluation usually relies on signals from only a few thermocouples. In practice, however, the number of thermocouples cannot be increased without limit because it is constrained by the number of measurement channels in the profiling system, sensor placement and attachment, and the time and labor required for wiring and measurement preparation. This motivates methods that reconstruct the PCB surface-temperature distribution from a small number of point measurements. Analytical, finite-element, and experimental studies of the reflow process have all shown that geometry, material properties, heat-transfer conditions, and measurement design substantially affect the observed temperature [1–4].

Check for updates

Academic Editor: Dan Zhang

Received: 28 September 2026
Revised: 7 November 2026
Accepted: 20 November 2026
Published: 24 November 2026

Copyright: © 2026 by the authors. Licensee MDPI, Basel, Switzerland. This article is an open access article distributed under the terms and conditions of the Creative Commons Attribution (CC BY) license.

Detailed reflow models describe temperature evolution from the thermal load and assembly properties. Whalley [1] examined a simplified process model, Van Steenberge et al. [2] developed analytical and finite-element descriptions, and Esfandyari et al. [3] investigated optimization combining simulation and experimental verification. Ran et al. [5] coupled sensitivity analysis and robust optimization with a finite-element reflow model while accounting for variations in oven settings and material properties. In addition to geometry, these approaches require physical parameters and a description of the thermal load. Interpretation of measurements is further complicated by the result of Straubinger et al. [4], who showed that thermocouple construction influences the observation of heat transfer. Spatial reconstruction from sparse point measurements must therefore consider both model simplifications and sensing limitations.

Data-driven optimization of process settings uses different information. Zhang et al. [6] combined a neural network aligned with the stages of reflow with mixed-integer linear optimization. Their method, which was based on thermocouple time series, was also tested on a different oven configuration, although the study focused on small passive components. Li et al. [7] used a random-forest model trained on experimental data to predict a defect metric derived from optical inspection and then applied it to oven-recipe optimization. These studies address the relationships among process settings, thermal profiles, and manufacturing quality. The task addressed here is the spatial reconstruction of temperatures measured at a given instant; by itself, it does not provide a quality assessment or a process-optimization result.

Field reconstruction from sparse measurement points is an underdetermined inverse problem: several different complete fields may be consistent with the same small set of measured values. A unique solution can be obtained only by introducing an additional assumption. This assumption may be derived from the differential equation of heat conduction, presumed field smoothness, a low-dimensional basis obtained from earlier simulations or measurements, or statistical relationships identified from training data. The essential differences among method families are therefore determined not only by reconstruction error, but also by the required prior information, treatment of geometry, computational cost, and transferability to new operating states.

In electronics thermal management, Ye et al. [8] investigated rapid full-field reconstruction from discrete measurement points, while Yuan et al. [9] analyzed the combined role of sensor layout and data-driven reconstruction in steady-state and transient thermal problems. These studies represent the class of tasks in which a small amount of current measurement data is supplemented by additional model or field information. When comparing them with the present method, it is therefore necessary to distinguish not only the number of input points but also whether the spatial information required for reconstruction originates from prior field samples or directly from a fixed spatial operator.

Direct interpolation can also be applied without a prior field database. Shepard's inverse distance weighting (IDW) [10] reconstructs unmeasured points from a distance-dependent average of the measured values. In the Euclidean-distance variant used in the present comparison, points on opposite sides of a cutout may be treated as close even when their connection within the domain is long or interrupted. This is a limitation of the selected distance metric, not a property of every IDW variant. Jara-Arriagada and Stoianov [11] examined graph-Laplacian interpolation and distance-based methods in a water-network application while also considering the role of network connectivity. Their results motivate a comparison of topology-aware methods, but they do not establish a general accuracy advantage for harmonic interpolation.

Zhu et al. [12] provided the theoretical basis of harmonic graph interpolation using both energy minimization and a resistor-network analogy. With fixed nodal values, every

unknown value is the weighted average of its connected neighbors. Narang et al. [13] studied interpolation of signals on graphs, and Shi et al. [14] examined a weighted nonlocal Laplacian operator; these belong to a broader family of methods than the regular four-neighbor grid used here. Within this framework, the resistor-network (RN) method enforces spatial smoothness through cell connections while preserving measured values. Cutouts are handled by omitting connections. The mathematical graph interpretation alone, however, does not demonstrate that the reconstructed field follows the complete physical temperature distribution of the reflow process.

Everson and Sirovich [15] addressed the reconstruction of incomplete data using a Karhunen–Loève basis, and Willcox [16] applied the gappy proper orthogonal decomposition (Gappy POD) approach to the sensing and reconstruction of time-dependent flow fields. In this family of methods, the field is approximated by a linear combination of a small number of dominant modes, whose coefficients are determined from measurement data. In thermal applications, Jiang et al. [17] coupled a POD-based reduced-order model with sparse sensor data, whereas Wang et al. [18] combined Gappy POD with a genetic algorithm for data-driven thermal-field reconstruction. Rapid online evaluation is thus enabled by a basis constructed from prior field information. By contrast, the basis vectors of the resistor-network influence-matrix method (RN-IM) are the unit-excitation responses of each sensor on the fixed graph; consequently, their construction does not require a representative library of measured or simulated fields.

The separation of preprocessing and online computation also appears in physics-based inverse models. Nassiopoulos and Bourquin [19] reconstructed a three-dimensional transient thermal field from time series of point temperature measurements. They stabilized identification of the unknown boundary load using Tikhonov regularization; the dual formulation and precomputed finite-element response fields shifted a substantial part of the computational demand to preprocessing. The method was verified on two simulation examples, including an analysis of measurement noise. Its application requires physical model parameters and temporal measurement data. The RN-IM produces a two-dimensional harmonic field from simultaneous point measurements, and its lower model and data requirements are achieved by omitting transient heat conduction and boundary-load identification. Thus, despite a shared precomputation principle, the inverse problems being solved differ.

Among direct interpolation methods, Guo et al. [20] performed real-time thermal-field reconstruction from a small number of measurement points using RPIM-AGQ6 point interpolation. Cao et al. [21] investigated an optimized Gaussian radial-basis-function network for two-dimensional thermal fields. Zhou et al. [22] applied a reflected sigmoid radial-basis function and QR decomposition to acoustic temperature reconstruction. In the latter case, the measurement information is associated with acoustic paths and therefore differs from interpolation of point thermocouple values. When these studies are compared, both the basis and its parameters, as well as the measurement operator, must be considered; errors reported for different tasks cannot be used to establish a direct accuracy ranking.

Learning-based methods supplement missing spatial information with the statistical structure of prior fields. Fukami et al. [23] combined sparse observations preprocessed by Voronoi tessellation with deep learning, whereas Santos et al. [24] developed the attention-based Senseiver architecture. These approaches also offer ways of handling varying observation locations; irregular sampling is therefore not an exclusive advantage of graph interpolation. Relative to the RN-IM, the essential difference lies in the field data required for training and in the domain over which the learned relationships remain applicable.

A study close to the present PCB application was reported by Sabathiel et al. [25]. The authors reconstructed steady-state thermal fields using a neural network trained on finite-

element simulations and then evaluated the method on sparse samples taken from infrared images of resistively heated PCBs. In the reported comparison, the network reconstructed temperature maxima more accurately than the selected Kriging variant, although boundary-only sampling was insufficient to reveal some internal hot spots. The representativeness of the training set remained a condition of applicability. The RN-IM operates without prior field samples, but its harmonic interpolation likewise cannot recover internal extrema that are absent from the measurements. Lower data requirements therefore do not automatically imply more accurate reconstruction, and a steady-state PCB experiment cannot be regarded as reflow validation.

Regardless of the selected method, sensor locations determine the available spatial information. Manohar et al. [26] combined a basis derived from prior field samples with QR-based selection. Liu et al. [27] proposed physics-based sensor placement for a setting in which an extensive field database was unavailable for placement design. The data requirements of the placement criterion must, however, be considered separately from those of the subsequent reconstruction. The present case study uses a fixed industrial sensor layout; placement optimization is therefore a subject for further investigation.

When comparing the investigated methods, the reconstruction objective, prior-information requirements, and validation type must be evaluated together. Physics-based inverse models may use temporal data and material parameters; POD and neural methods construct their representations from prior fields; and direct interpolation methods supplement instantaneous measurements using a selected spatial rule. The RN belongs to the latter group. Here, the harmonic condition is a spatial regularization assumption, not evidence that the PCB moving through the oven is physically in a steady state. The benefit of lower information requirements must therefore be considered together with the limited description of spatially varying material structure, heat storage, and unmeasured local extrema.

The acceleration of linear reconstruction through precomputation also has direct precedents in image processing. Peter et al. [28] reconstructed images as weighted sums of diffusion response fields associated with unit values at known pixels. For fixed Dirichlet locations, Jumakulyyev and Schultz [29] constructed a matrix from unit-vector finite-element responses, thereby transforming repeated evaluation into a matrix–vector product. This is a close mathematical analogue of RN-IM precomputation. Image-compression applications do not establish thermal accuracy, but they demonstrate that the general principles of linearity, a unit-excitation basis, and offline–online decomposition are established.

Recent work also combines graph structure with learned thermal representations. Li et al. [30] developed a physics-embedded graph neural network (PEGNN) whose layers use heat-diffusion and finite-difference operators on a graph. Their evaluation included comparisons with neural baselines and tests involving distribution shifts. PEGNN therefore uses graph connectivity within a learned reconstruction, whereas the present RN applies a fixed harmonic averaging rule without network training. These are different uses of graph structure, and their errors cannot be ranked from results on different datasets.

Su et al. [31] combined graph-Laplacian regularization with POD and graph-autoencoder representations for sparse temperature observations in data centers. The graph was based on CFD mesh connectivity, and the evaluation varied sensor numbers and observation noise. This approach combines a reduced representation with a spatial prior. RN-IM instead precomputes the response of each fixed sensor in the specified harmonic model; it does not extract thermal modes from a field database. This reduces the need for prior field data, while its accuracy here is assessed only at the five omitted sensor locations.

Building on this background, the present study examines a specific application: spatial reconstruction from a small number of simultaneous PCB thermocouple values, followed

by acceleration of repeated evaluations for the same grid and sensor layout. The RN-IM stores responses precomputed for the fixed sensor locations of the graph and maps each new measurement vector to the complete grid through their linear combination. The contribution is the implementation and evaluation of established harmonic reconstruction and linear precomputation in a PCB reflow case study. The investigation therefore focuses on reconstruction errors that can be checked at measurement points, the role of connectivity, and the number of evaluations required to amortize preprocessing cost.

The aim of this study is to investigate a reproducible, measurement-based resistor-network reconstruction and its influence-matrix evaluation. The accuracy results should be interpreted as a case study for a single measurement state. The numerical agreement between the RN and RN-IM verifies reproduction of the applied linear mapping; an independent spatial reference would be required to determine the accuracy of the complete physical field.

The main contributions are as follows:

(i) implementation of harmonic, resistor-network-based surface reconstruction from seven measured PCB temperatures;
(ii) leave-one-out validation at five selected sensors and comparison with Euclidean IDW interpolation using $p = 2$ as the main reference setting, with an additional sensitivity comparison at $p = 1$ and $p = 3$;
(iii) investigation of the effect of cell connectivity on a synthetic concave domain; and
(iv) evaluation of an influence matrix constructed from unit excitations in terms of numerical agreement with direct iteration, online runtime, and preprocessing break-even point.

2. Materials and Methods

2.1. Investigated PCB and Measurement Data

The investigation was based on a measurement state recorded during an industrial reflow-soldering process. Seven K-type thermocouples measured local temperatures on the surface of a printed circuit board (PCB) measuring approximately 10 × 15 cm. An additional thermocouple recorded the surrounding air temperature, but it was not used in the two-dimensional surface reconstruction because it did not represent a boundary or internal condition associated with a point on the board. The thermocouple used to measure the surrounding air was designated as sensor 1 in the original profiling system; consequently, the seven surface thermocouples retained their original identifiers 2–8. The surface thermocouples were accuracy class 1, with a nominal accuracy of ±1.5 °C. Under the company's confidentiality restrictions, the manufacturers and exact models of the sensors and profiling system, thermocouple wire diameters, and sensing-junction construction and dimensions were not made available to the authors. This lack of technical documentation limits the assessment of the measurement configuration and its associated uncertainty. Reference [4] provides background on how thermocouple construction affects measurement response; its citation does not indicate that the sensor construction or measurement arrangement described in that study was used to acquire the present dataset.

The company's technical specialists selected the measurement locations and soldered the seven surface thermocouples to these points on the PCB, taking into account the locations of cold and hot spots and critical components. Sensor placement was outside the scope of the present research, which used the supplied measurements to reconstruct the surface-temperature field.

Figure 1 shows the investigated PCB with the 10 × 15 computational grid and the grid cells assigned to the seven surface thermocouples. Due to the company's confidentiality requirements, the PCB photograph is reproduced only in the blurred form authorized for

publication. The sensor identifiers and their grid-cell locations remain clearly indicated and correspond to those listed in Table 1.

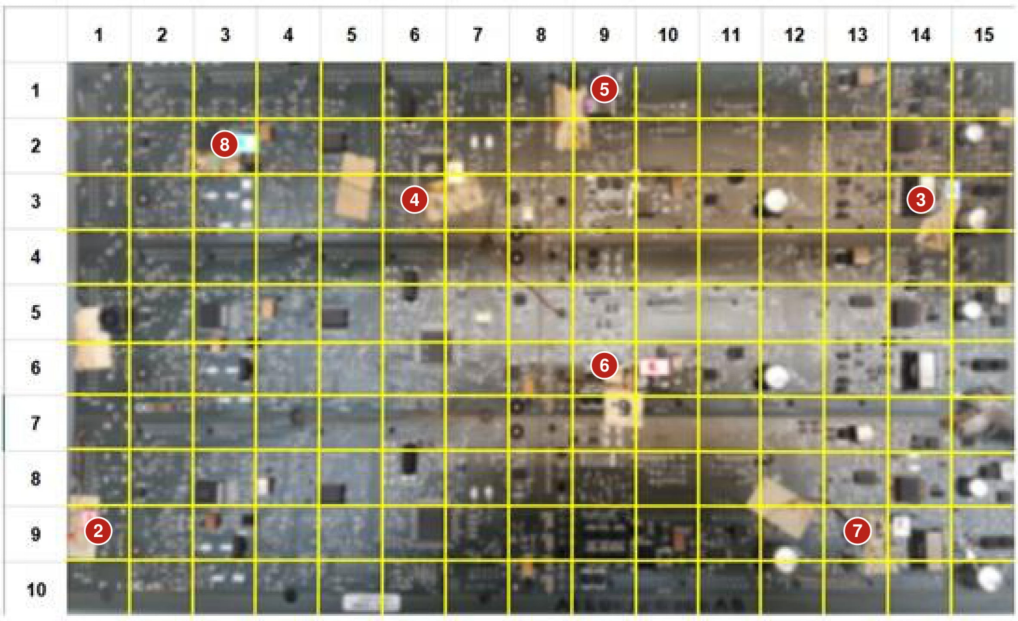


Figure 1. Investigated PCB with the 10 × 15 computational grid. Numbered markers (2–8) identify the grid cells assigned to the seven surface thermocouples, as listed in Table 1. The PCB photograph is reproduced in the blurred form authorized by the company to protect confidential technical information.

Table 1. Measurement points used for surface reconstruction.

Sensor	Grid Row	Grid Column	Temperature (°C)
2	9	1	250
3	3	14	242
4	3	6	246
5	1	9	243
6	6	9	241
7	9	13	242
8	2	3	243

The available dataset contained seven surface temperatures from one representative instant selected within the soldering zone. All input values corresponded to the same measurement time; hence, the reconstruction began from a simultaneous spatial state. The dataset did not contain a complete time-resolved thermal profile for every sensor. Accordingly, the purpose of the study was not to simulate the transient thermal process of a PCB passing through the oven, but to reconstruct the surface-temperature distribution at the selected instant. This single measurement state served as the input to both the resistor-network and IDW reconstructions in the methodological comparison.

The seven temperatures ranged from 241 to 250 °C. The measurement points did not form a regular sampling grid: sensors were located both near the board edges and in interior regions, while no direct measurement was available in most grid cells. Because of the sparse sampling, the complete field cannot be determined uniquely from the data alone; the selected spatial model relates the values of the unknown cells. Table 1 summarizes the sensor identifiers, their positions on the discretized grid, and the temperatures supplied to the reconstruction.

The measured temperatures were not filtered, smoothed, or corrected after acquisition. This ensured that the reconstruction methods were compared using the same unchanged input. Nevertheless, the nominal measurement uncertainty of the thermocouples sets a lower bound on the interpretation of achievable physical accuracy: numerical differences of tenths or thousandths of a degree in the calculated values cannot be equated with physical measurement accuracy of the same magnitude. Owing to the absence of a larger number of repeated measurements and of a complete time profile, this study primarily examines the operation of the reconstruction principle, geometric treatment, and computational acceleration.

2.2. Computational Domain and Mapping of Measurement Points

The PCB surface was represented by a rectangular grid with 10 rows and 15 columns, comprising 150 cells. Based on the approximate board dimensions of 10 × 15 cm, one cell corresponded to a surface area of approximately 10 × 10 mm. Row indices increased from top to bottom and column indices from left to right. The grid resolution was selected to match the available geometric information and sparse sensor layout; its purpose was not to resolve component-scale temperature gradients but to provide a medium-resolution, reproducible surface field.

Each surface thermocouple was mapped to the grid cell nearest its physical position. After mapping, the temperature of that cell remained fixed at the measured value throughout the computation; thus, sensor cells acted as internal Dirichlet conditions. If several measurements were assigned to the same cell, a separate aggregation rule would be required; in the investigated layout, however, every sensor occupied a distinct cell. The temperatures of the remaining 143 cells were treated as unknowns on the rectangular domain.

To examine geometric handling, a synthetic concave computational domain was created in addition to the complete rectangle. In this domain, the 18 cells at the intersections of grid rows 5–10 and columns 4–6 were excluded from the computation. The mask therefore created a stepped cutout extending from the lower-left region without removing any measurement point. The concave variant is not a geometric reproduction of a particular PCB cutout; it is a test case used to examine whether the method transmits temperature influence exclusively through cells that are actually connected.

Figure 2 presents both computational domains and the discrete sensor locations. Geometry was supplied to the program as a binary mask: active cells participated in the system of equations, whereas removed cells had neither a temperature nor neighborhood connections. This representation can readily be extended to other outlines, cutouts, or excluded regions, provided they can be described by a cell mask at the selected grid resolution. Together, the grid resolution, mask, and sensor locations define the graph used subsequently and the validity range of the influence matrix.

2.3. Model Assumptions and Boundary Conditions

Each measurement instant can be treated as an independent, two-dimensional, quasi-steady-state reconstruction problem. The model assumes a homogeneous surface with effective in-plane thermal-conduction properties and no separately specified volumetric or surface heat source within the unknown domain. The layered PCB structure, local distribution of copper foil, thermal capacitance of components, convective and radiative heat exchange with the oven environment, and through-thickness temperature differences do not appear as separate parameters. Their effects are represented only indirectly through the measured values and the assumption of homogeneous effective propagation.

Under these assumptions, the continuous counterpart of the smooth temperature field sought in the unmeasured region is described by the Laplace equation:

$$\nabla^2 T = 0 \tag{1}$$

where T is the surface temperature. Equation (1) is not intended to replace the complete energy balance of the reflow process; rather, it is a regularizing spatial model that selects a harmonic field between the measurement points without introducing an artificial internal source or sink. The solution therefore matches the sensor values exactly and provides a smooth transition at unknown locations as determined by local connectivity.

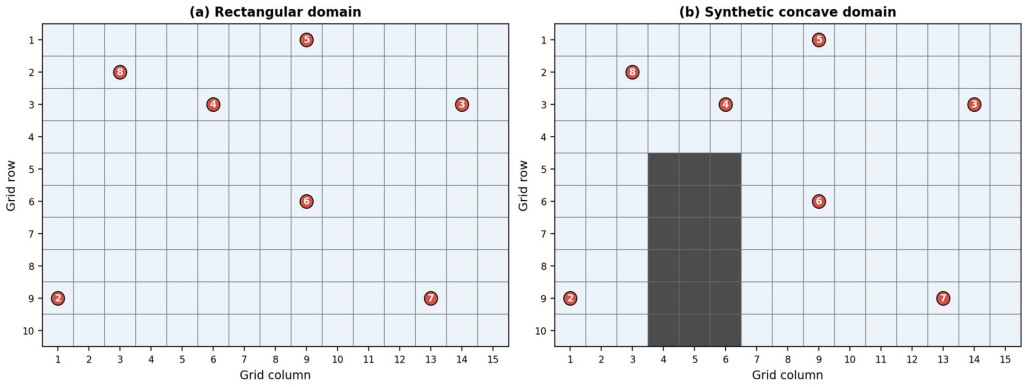


Figure 2. Mapping of the computational domain and measurement points: (**a**) the 10 × 15 cell rectangular grid; (**b**) the synthetic concave domain. Numbered circles indicate the seven surface measurement points, and gray cells indicate the region excluded from the computation.

The discretized surface can be treated as a resistor network (RN). Grid cells are the network nodes, and thermal connections are assigned between active cells that share an edge [11–14]. The steady-state balance at node i can be written as a zero sum of the heat flows transferred through all neighboring branches:

$$\sum_{j \in N(i)} g_{ij}\left(T_i - T_j\right) = 0 \tag{2}$$

where $N(i)$ is the set of active cells sharing an edge with cell i, g_{ij} is the effective conductance between cells i and j, and T_i and T_j are the nodal temperatures. In this study, all active connections were assigned the same g_{ij} value. Because the equation is homogeneous, the common conductance cancels, and the temperature of an unknown cell is therefore the arithmetic mean of its existing neighbors:

$$T_i = \frac{1}{d_i} \sum_{j \in N(i)} T_j \tag{3}$$

where $d_i = |N(i)|$ is the number of active neighbors. Interior cells of the complete rectangle have four neighbors, whereas cells on the external boundary have two or three. At the boundary of the concave mask, only cells that actually exist are included in the average; no separate external temperature is prescribed in the direction of removed cells. In the graph model, this corresponds to a reflecting, zero-normal-heat-flux boundary. Sensor cells, by contrast, are not averaged but form internal boundary conditions fixed at the measured values.

Owing to the maximum principle for harmonic solutions—on a connected domain with at least one fixed cell—the values of unknown cells cannot exceed the minimum or maximum of the specified sensor temperatures. This is an important numerical check, although it does not demonstrate the physical accuracy of the reconstructed field. The model can represent a local thermal peak only if it is fixed by a measurement point or introduced through an explicit source term. Consequently, the RN field is a harmonic interpolation of the available sparse data rather than a detailed thermal digital twin.

2.4. Matrix Formulation

The grid and cell mask define an undirected graph. An element of the graph adjacency matrix A equals 1 if two active cells share an edge and 0 otherwise; the diagonal elements of the degree matrix D contain the number of neighbors d_i for each cell. The discrete Laplacian is given by $L = D - A$. The nodes can be divided into two sets: the measured sensor cells M and the unknown cells U. After the corresponding reordering of rows and columns, the equations for unmeasured cells are

$$L_{uu}T_u = -L_{um}T_m \tag{4}$$

where T_u is the temperature vector for unknown cells and T_m is the vector for measured cells; L_{uu} is the unknown–unknown submatrix, and L_{um} contains the connections between unknown and measured cells. The measured values appear on the right-hand side; therefore, the solution is a linear function of the input vector T_m. The matrix L_{uu} is nonsingular if every connected component contains at least one fixed sensor cell, which was true for the connected domains investigated here. The Dirichlet problem therefore has a unique solution.

The matrix form separates measurement data from geometric structure. The blocks of L depend only on the grid, mask, neighborhood rule, and locations of measured cells; current temperature values appear only in T_m. This separation forms the basis of the offline–online decomposition: for a fixed geometry, the geometry-dependent mapping can be precomputed once and then evaluated rapidly for new measurement vectors.

The converged discrete solution can formally be written as $T_u = -{L_{uu}}^{-1}L_{um}T_m$. This relationship demonstrates linear dependence on the sensor values; however, the program did not form an explicit inverse and instead used a simple local iteration that is also transparent in a spreadsheet environment. Construction of the influence matrix used the same iterative operator, ensuring that the comparison between the accelerated and baseline methods was not affected by different linear solvers.

2.5. Iterative Numerical Solution and Implementation

The baseline RN problem was solved numerically using Jacobi iteration. Unknown cells were initialized to 0 °C, while sensor cells contained the measured temperatures from iteration zero. During each complete iteration, the new value of every unknown cell was calculated exclusively from active-neighbor values stored in the preceding iteration state:

$$T_i^{(k+1)} = \frac{1}{d_i}\sum_{j\in N(i)} T_j^{(k)} \tag{5}$$

where k is the iteration index and $i \in U$ denotes an unknown cell. After every step, the program reset the sensor-cell values to their input values; therefore, the iteration could not modify the measurement conditions. The new and previous fields were stored in separate arrays, ensuring that cells already updated within an iteration did not influence subsequent calculations belonging to the same step. This distinguishes the applied Jacobi scheme from a sequential Gauss–Seidel update.

Numerical convergence was monitored using the largest absolute change over the unknown cells between two consecutive iterations:

$$\Delta T_{\max}^{(k)} = \max_{i\in U}\left|T_i^{(k+1)} - T_i^{(k)}\right| \tag{6}$$

Based on the preceding convergence study, every final reconstruction used a fixed value of $K = 500$ iterations. For the seven-sensor baseline reported in Table 2, ΔT_{max} was 0.00003 °C at this point. This stepwise change indicates stabilization of that iteration; it is not a bound on the remaining solution error for every configuration. The fixed iteration count also ensured identical numerical treatment of the baseline case and the basis fields.

The 0 °C initial value affects only the convergence path; the converged harmonic solution depends on the fixed boundary values and graph.

Table 2. Convergence and runtime of the RN procedure.

Iterations	ΔT_{max} (°C)	Runtime (s)
100	0.90921	0.00336
200	0.06913	0.00648
500	0.00003	0.01680

The computations were implemented in Microsoft Excel for Microsoft 365 using Visual Basic for Applications (VBA). The cell mask, sensor locations, and temperatures were transferred from worksheet ranges to arrays held in memory, and the complete field could be written back in tabular form after reconstruction. Runtime measurements were performed on an HP EliteBook x360 830 G8 (HP Inc., Palo Alto, CA, USA) running Windows 11 Enterprise, equipped with an Intel Core i5-1145G7 processor (2.60 GHz, 4 cores/8 threads) (Intel Corporation, Santa Clara, CA, USA) and 16 GB of memory.

All reported runtimes are arithmetic means of 100 consecutive runs. Timing covered the corresponding algorithmic section; opening Excel, loading the workbook, and user interaction were excluded. Absolute values are platform-dependent because of the timing resolution of VBA and the operating system; consequently, the acceleration ratios apply to the implementation used here. Nevertheless, use of the same hardware, file, and software environment enabled an internal comparison of the direct RN method, preprocessing, and online matrix multiplication.

2.6. Influence-Matrix Acceleration

According to Equation (4), the reconstructed field depends linearly on the sensor temperatures when the geometry, neighborhood connections, sensor locations, and iteration parameters remain unchanged. To exploit this property, the RN-IM was formulated. A separate unit-excitation basis problem was created for each sensor $s = 1, \ldots, m$. In the s-th problem, the value of that sensor was 1 and all other sensor values were 0, while unknown cells were assigned the same zero initial value as in the baseline case. Each basis field was generated using 500 Jacobi iterations.

The complete cell vector $w^{(s)}$ obtained from the s-th unit excitation describes the weight with which a unit temperature at the corresponding sensor appears at every point of the network. Arranging the seven basis vectors as columns yields the influence matrix W. The current complete field can then be calculated as a linear combination of the actual sensor values:

$$W = \left[w^{(1)}\ w^{(2)}\ \ldots\ w^{(m)} \right], \qquad T = WT_m \tag{7}$$

where $m = 7$, T_m is the column vector of sensor temperatures, and T contains the reconstructed temperatures of all active cells. Rows of W corresponding to measured cells are the unit vectors of the relevant sensors; therefore, matrix multiplication reproduces the measured values unchanged. The weights of unknown cells are nonnegative, and as the iteration converges, their sum approaches 1 in every row. Individual cell temperatures can thus be interpreted as convex combinations of the sensor values. No post hoc row normalization was applied; equality was ensured exclusively by the superposition property of the identical linear iteration.

Constructing the influence matrix is an offline stage that requires m independent RN runs and is therefore more expensive than a single direct reconstruction. Once it has been constructed, however, online evaluation of a new measurement state consists only of the matrix–vector product WT_m. The accelerated variant is particularly advantageous when

many time instants or manufacturing cycles must be processed for the same PCB geometry and unchanged sensor layout.

For identical initial values and iteration counts, a linear combination of the 500-step basis fields gives the same finite-iteration result—within floating-point rounding—as a direct 500-step RN run. Numerical identity was assessed using the maximum cell-wise absolute difference between the two complete fields. The W matrix must be regenerated if the grid, cell mask, neighborhood or conductance model, location of any sensor, iteration count, or iteration scheme changes. A change only in the measured temperature values does not require new preprocessing.

2.7. IDW Reference Interpolation

The results of the RN reconstruction were compared with inverse distance weighting (IDW) interpolation [10]. IDW does not impose grid-neighborhood equilibrium; the temperature at a target point is obtained as a distance-dependent weighted average of all available sensor values. The interpolated value at the center of target cell x is

$$\hat{T}(x) = \frac{\sum_{s=1}^{m} d(x, x_s)^{-p} T_s}{\sum_{s=1}^{m} d(x, x_s)^{-p}} \tag{8}$$

where x_s is the center of the s-th sensor cell, $d(x, x_s)$ is the Euclidean distance, and p is the distance exponent. If the target cell was a sensor cell, the program returned the measured value T_s directly to avoid the singularity associated with zero distance. The main comparison retains $p = 2$, which gave a lower MAE than $p = 1$ for the five omission cases. Sensitivity to the exponent was assessed at $p = 1$, 2, and 3 using the same omitted sensors and all six retained measurements in each case. Smaller positive exponents give distant sensors greater relative weight, whereas larger exponents emphasize nearby sensors. These settings provide a limited sensitivity comparison rather than an exhaustive optimization; $p = 2$ is not assumed to be optimal across error metrics.

Both methods used the same sensor data, grid-cell centers, and active-cell mask. An important geometric difference, however, is that IDW weights are determined by the straight-line distance between two points, and this distance does not follow connectivity paths in a concave domain. Thus, cells on opposite sides of a cutout that are close in the Euclidean sense may indirectly exert a strong influence on one another even if they are connected only through a longer detour in the grid graph. The RN, by contrast, transmits sensor influence exclusively through active edge-adjacent cells.

2.8. Validation and Error Metrics

Predictive accuracy was evaluated using leave-one-out validation at each internal measurement point. In each validation run, the temperature of one internal sensor was omitted from the input conditions; its cell became unknown, and the field was reconstructed from the remaining six sensors. The value reconstructed at the omitted location could then be compared with the actually measured value, which had been withheld from the reconstruction. The same sensor set was used for the RN and IDW reconstructions.

The two extreme sensors recording the global minimum and maximum remained part of the input in every run. This was necessary because the harmonic RN solution remains within the range of the available Dirichlet values; omitting an extreme value would therefore change not only the internal prediction being tested but also the admissible value range. The procedure yielded $n = 5$ omission cases. Thus, it was not a complete leave-one-out cross-validation covering every sensor, but a test restricted to internal measurement points.

The signed error for omission case q was defined as the difference between the reconstructed and measured temperatures:

$$e_q = \hat{T}_q - T_q \tag{9}$$

A positive signed error indicates a reconstructed value above the measurement, and a negative error indicates a value below it. The five cases were summarized using the mean absolute error (MAE), root mean square error (RMSE), maximum absolute error, and mean bias error (MBE):

$$\begin{aligned} \mathrm{MAE} &= \frac{1}{n}\sum_{q=1}^{n}\left|e_q\right|, \quad \mathrm{RMSE} = \sqrt{\frac{1}{n}\sum_{q=1}^{n} e_q^2}, \\ e_{\max} &= \max_q\left|e_q\right|, \quad \mathrm{MBE} = \frac{1}{n}\sum_{q=1}^{n} e_q \end{aligned} \tag{10}$$

The MAE provides an easily interpretable magnitude of the mean deviation, the RMSE gives greater weight to large errors, the maximum absolute error identifies the least favorable investigated case, and the MBE indicates the mean direction of deviation. Because of the small sample size of $n = 5$, these are descriptive measures and do not support population-level statistical inference. Differences between the complete fields of the two methods over all active cells were likewise characterized by the RMSE and the maximum cell-wise absolute difference. These full-field measures are not independent measurement errors because no reference temperature was available at nonsensor locations; they quantify only the magnitude of the difference between the RN and IDW methods.

2.9. Computational Performance and Break-Even Number of Evaluations

Three times were distinguished in the performance evaluation: t_{RN}, the time required for direct RN reconstruction of one measurement state; t_{pre}, the one-time duration required to construct the influence matrix W; and ton, the online matrix-multiplication time for a new T_m vector. The speed ratio between direct and online evaluation and the break-even number of evaluations accounting for preprocessing were calculated as follows:

$$S = \frac{t_{\mathrm{RN}}}{t_{\mathrm{on}}}, \qquad N_{\mathrm{BE}} = \mathrm{ceil}\left(\frac{t_{\mathrm{pre}}}{t_{\mathrm{RN}} - t_{\mathrm{on}}}\right) \tag{11}$$

where S is the acceleration factor and N_{BE} is the smallest integer number of new measurement states at which the total time of the influence-matrix method is no greater than that of repeated direct RN runs. The expression follows by rearranging $t_{\mathrm{pre}} + \mathrm{N}{\cdot}t_{\mathrm{on}} \le \mathrm{N}{\cdot}t_{\mathrm{RN}}$. A finite break-even point exists only if $t_{\mathrm{on}} < t_{\mathrm{RN}}$; otherwise, preprocessing is not amortized in terms of computational time.

The comparison was performed for 100, 200, and 500 Jacobi iterations to show the different scaling of the accuracy cost of the baseline case and the online cost of the influence matrix. Evaluation of the final reconstruction was based on the 500-iteration setting. Preprocessing consists of m basis problems; consequently, its time is approximately proportional to the number of sensors and iterations. By contrast, the online stage multiplies a matrix of size number of active cells × number of sensors by a short vector.

The reported runtimes apply to the Excel/VBA code and hardware used in this study. A different programming language, an optimized linear-algebra library, a different grid size, or a larger number of sensors would change the absolute times and acceleration ratio. The break-even number of evaluations is therefore not a universal constant, but a practical decision metric for the specified configuration. The methodological conclusion is that, for unchanged geometry, the computation can be decomposed into one-time offline preparation and repeated online evaluation at very low cost.

3. Results

3.1. RN Field and Convergence of the Iterative Solution

The resistor-network field calculated using 500 iterations remained within the 241–250 °C range defined by the measured minimum and maximum in every active grid cell. The highest temperature occurred near sensor 2, and the lowest value at sensor 6. No local maximum above 250 °C or minimum below 241 °C was produced in unmeasured cells. This agrees with the maximum principle for the discrete harmonic solution and also confirms that the numerical application of boundary and sensor conditions did not create artificial overshoot or undershoot.

Figure 3 presents the RN field obtained after 500 iterations and the IDW field generated from the same seven measurement points using $p = 2$, both on the same color scale of 241–250 °C. Both reconstructions provide gradual spatial transitions between the fixed measurements, although their local distributions differ because of their distinct mathematical bases. The numerical 10 × 15 matrices for the RN and IDW fields are reported in Tables A1 and A2, respectively.

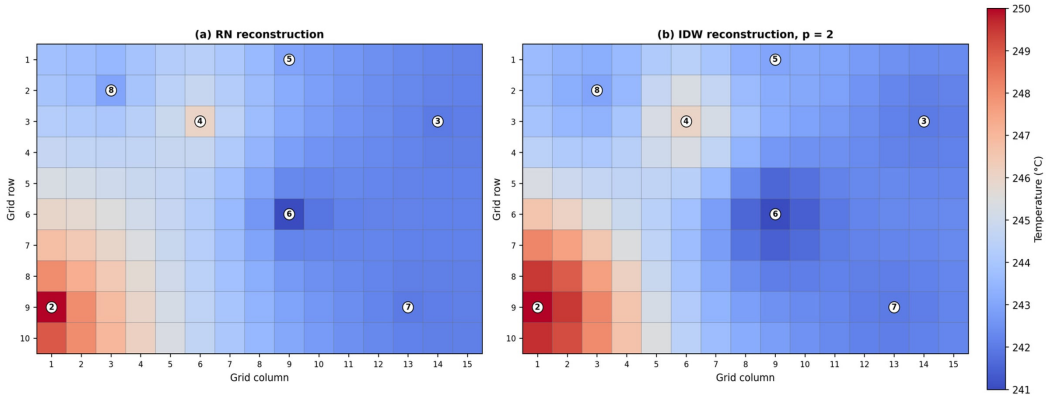


Figure 3. Reconstructed surface-temperature distribution over the complete rectangular domain: (**a**) RN method after 500 Jacobi iterations; (**b**) IDW interpolation with $p = 2$. Both panels use the same color scale of 241–250 °C; numbered circles indicate the seven thermocouple measurement locations.

Convergence of the Jacobi iteration was characterized by the largest cell-wise temperature change between two consecutive fields. As shown in Table 2, after 100 iterations this value was still 0.90921 °C, and the field could not yet be regarded as numerically converged. At 200 iterations, the maximum change had decreased to 0.06913 °C; at 500 iterations, it was only 0.00003 °C. The reduction between 100 and 500 iterations was greater than a factor of 30,000, showing strong attenuation of the stepwise update in this baseline configuration.

Runtime increased approximately in proportion to the iteration count. On average, 100 steps required 0.00336 s, 200 steps required 0.00648 s, and 500 steps required 0.01680 s. Increasing the iteration count by a factor of five therefore increased runtime by exactly the same factor, while reducing the residual change by more than four orders of magnitude. The mean time per iteration was approximately 3.3×10^{-5} s for all three settings, indicating that within the investigated range, computational cost was primarily determined by the number of grid updates performed.

Figure 4 illustrates the different scaling of convergence and runtime. The maximum change decreases across several orders of magnitude on the logarithmic axis, whereas runtime follows the iteration count approximately linearly. The 500-iteration setting was therefore used in the subsequent evaluation: it produced a numerically stable field, while the runtime of the baseline method remained on the order of hundredths of a second even in a direct spreadsheet environment.

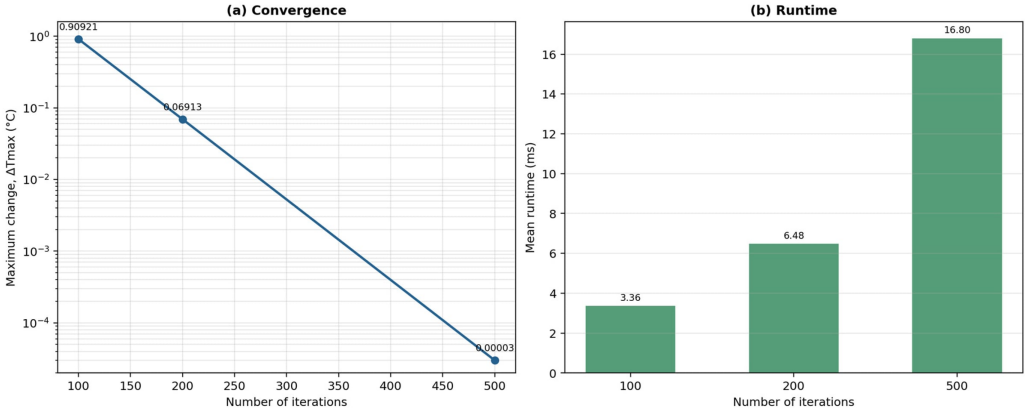


Figure 4. Convergence and computational time of the iterative RN solution: (**a**) maximum cell-wise change between two consecutive fields on a logarithmic scale; (**b**) mean runtime.

3.2. Pointwise Leave-One-Out Validation

Detailed results from omitting the five internal measurement points are reported in Table 3. Both methods reconstructed the temperature at the omitted point from the same six remaining sensor values. The signed error is the difference between the reconstructed and measured values; a positive value indicates a reconstruction above the measurement, and a negative value indicates a reconstruction below it. The sensors recording the global minimum and maximum were retained in every run; hence, the five cases tested interpolation within the original measurement range. Accordingly, the results characterize predictive behavior at internal points rather than extrapolation beyond the measured range.

Table 3. Detailed results of pointwise leave-one-out validation.

Sensor	Measured (°C)	RN Reconstruction (°C)	RN Error (°C)	IDW Reconstruction (°C)	IDW Error (°C)
3	242	242.52	+0.52	242.96	+0.96
4	246	243.17	−2.83	242.91	−3.09
5	243	243.46	+0.46	243.80	+0.80
7	242	242.45	+0.45	242.78	+0.78
8	243	245.70	+2.70	245.10	+2.10

The RN yielded a smaller absolute error than IDW at four of the five points. At sensors 3, 5, and 7, RN deviations remained between 0.45 and 0.52 °C, whereas IDW produced values 0.78–0.96 °C higher than the measurements at the same locations. For the 246 °C value at sensor 4, both methods yielded lower results: by 2.83 °C for the RN and by 3.09 °C for IDW. This was the largest negative error for both methods and indicates that the smooth field formed from sparse surrounding measurements could follow the locally elevated value only to a limited extent.

Sensor 8 was the only omission case in which the IDW absolute error was smaller: IDW produced a deviation of +2.10 °C and the RN a deviation of +2.70 °C. The difference between the two methods at this point was 0.60 °C in favor of IDW. The error signs followed the same pattern for both methods: positive deviations at four points and a negative deviation at one point. This indicates that the local behavior of the two reconstructions is not independent; the sensor layout and surrounding measured values induced deviations in the same direction for both methods, while the magnitudes differed.

For both methods, three of the five absolute errors remained below 1.5 °C, and two exceeded the nominal thermocouple accuracy. The ±1.5 °C value is not an acceptance limit for reconstruction, but the nominal accuracy of the thermocouples used. The validation

error therefore reflects the combined effects of reconstruction deviation and measurement uncertainty; given the small sample, the pointwise results primarily demonstrate the internal consistency of the specific measurement layout.

3.3. Aggregate Accuracy Comparison Between RN and IDW

The aggregate error metrics for the five omission cases are summarized in Table 4, including the IDW sensitivity settings $p = 1$ and $p = 3$. All metrics were calculated from unrounded predictions; the pointwise values in Table 3 are rounded for display. The MAE was 1.390 °C for RN and 1.545 °C for IDW with $p = 2$, a reduction of 10.04%. The corresponding maximum absolute errors were 2.826 and 3.086 °C, a reduction of 8.43%.

Table 4. Summary of validation error metrics and IDW exponent sensitivity (five omission cases).

Method	MAE (°C)	RMSE (°C)	Max. Abs. Error (°C)	Mean Bias (°C)
RN	1.390	1.785	2.826	+0.260
IDW, $p = 1$	1.609	1.748	2.839	+0.473
IDW, $p = 2$	1.545	1.795	3.086	+0.311
IDW, $p = 3$	1.533	1.905	3.206	+0.250

The difference between the root mean square errors was substantially smaller: the RMSE was 1.785 °C for the RN and 1.795 °C for IDW with $p = 2$, a difference of only 0.010 °C, or approximately 0.54%. This was because the two largest absolute errors were distributed in opposite ways: the RN was more favorable at sensor 4, whereas IDW was more favorable at sensor 8. Squaring gave substantial weight to both large deviations, so RMSE distinguished the two methods less clearly than MAE.

The mean signed error remained small and positive for both methods. The mean errors of +0.260 °C for the RN and +0.311 °C for IDW with $p = 2$ indicate a slight positive direction of deviation over the five investigated points. The approximately 0.051 °C difference is small relative to the nominal accuracy of the measurement system and cannot be generalized as systematic bias from a single measurement state. These results describe the comparison with IDW at $p = 2$ and do not imply superiority over other parameter settings.

The sensitivity results show a metric-dependent trade-off. Among the three IDW settings, $p = 3$ gave the lowest MAE (1.533 °C), whereas $p = 1$ gave the lowest RMSE (1.748 °C) and maximum absolute error (2.839 °C). Increasing p from 1 to 3 reduced MAE but increased RMSE and maximum error. RN had the lowest MAE of the compared settings, but its RMSE of 1.785 °C exceeded that of IDW with $p = 1$. Thus, $p = 2$ is a reference setting rather than an optimum across all criteria. These five cases support a descriptive sensitivity comparison, not an independent assessment of a parameter selected using those same cases.

Figure 5 presents the signed errors at each point. The bars for the two methods have the same sign at every sensor, and the largest deviations occur at the same two points. The dashed lines indicate the nominal thermocouple accuracy of ±1.5 °C; they are included as a guide to interpreting the measurement scale rather than as qualification limits. The chart also shows that the aggregate mean metrics comprise two larger and three notably small deviations.

3.4. Effect of Domain Topology

On the rectangular domain, the RMSE between the complete IDW and RN fields was 0.4797 °C, and the maximum cell-wise absolute difference was 1.6981 °C. On the synthetic concave domain, the RMSE increased to 0.5432 °C and the maximum difference to 1.8788 °C. Introducing the concave mask therefore increased the RMSE by 0.0635 °C, or 13.24%, and

the maximum difference by 0.1807 °C, or 10.64%. The methods already differed measurably on the rectangular domain, and the topological obstacle further amplified this difference.

The upper two panels of Figure 6 show the RN and IDW fields, and the lower panel shows the cell-wise IDW − RN difference. At measurement points, the two methods return the same values; therefore, the difference is zero. Different spatial weightings apply in unmeasured cells. RN influence propagates through the four-neighbor connections of active cells, and cells in the cutout interrupt direct connections. By contrast, IDW uses the Euclidean distance between a sensor and the target cell and may therefore treat points on opposite sides of the cutout as close despite the geometric mask.

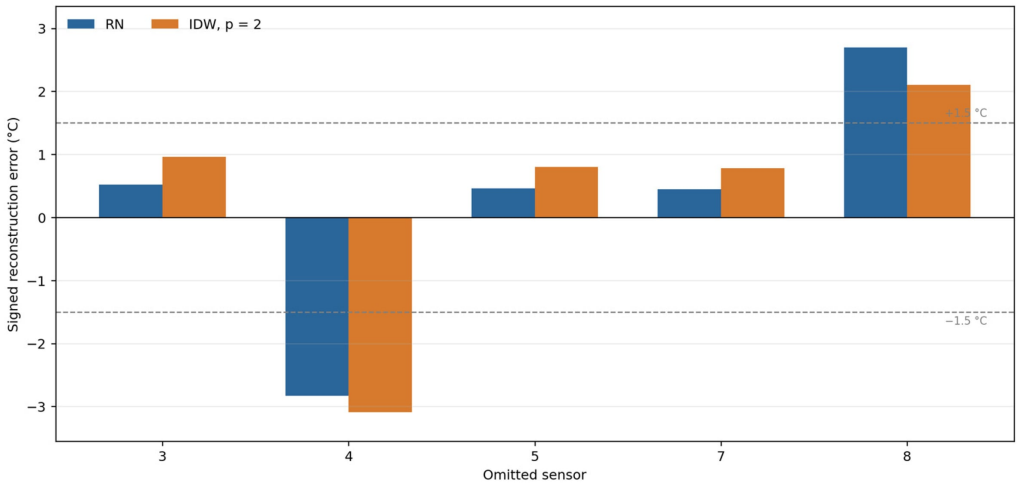


Figure 5. Pointwise signed errors of the RN and IDW ($p = 2$) when internal measurement points were omitted. Dashed lines indicate the nominal accuracy of ±1.5 °C for K-type, accuracy-class-1 thermocouples.

The largest positive values in the difference field occurred near the lower-right end of the cutout, whereas larger negative deviations occurred in several cells of the left-hand region. This spatial pattern is not a simple constant offset but results from the different topology sensitivity of the two interpolation principles. In the RN field, influence from sensors on the opposite side of the cutout is transmitted only along the detoured grid connections, whereas the IDW distance weight does not include this detour.

The metrics in Table 5 cannot be regarded as measurement errors because no independent reference temperature was available at nonsensor locations. Here, the RN is the comparison reference, and the RMSE and maximum characterize only the magnitude of the full-field difference between the methods. The concave example therefore quantitatively illustrates that explicit incorporation of domain shape measurably changes the reconstruction; by itself, however, it does not determine which complete field is closer to the unknown physical distribution on the actual PCB.

Table 5. Deviation of the complete IDW field from the RN reference.

Computational Domain	RMSE (°C)	Max. Abs. Difference (°C)
Rectangle	0.4797	1.6981
Synthetic concave	0.5432	1.8788

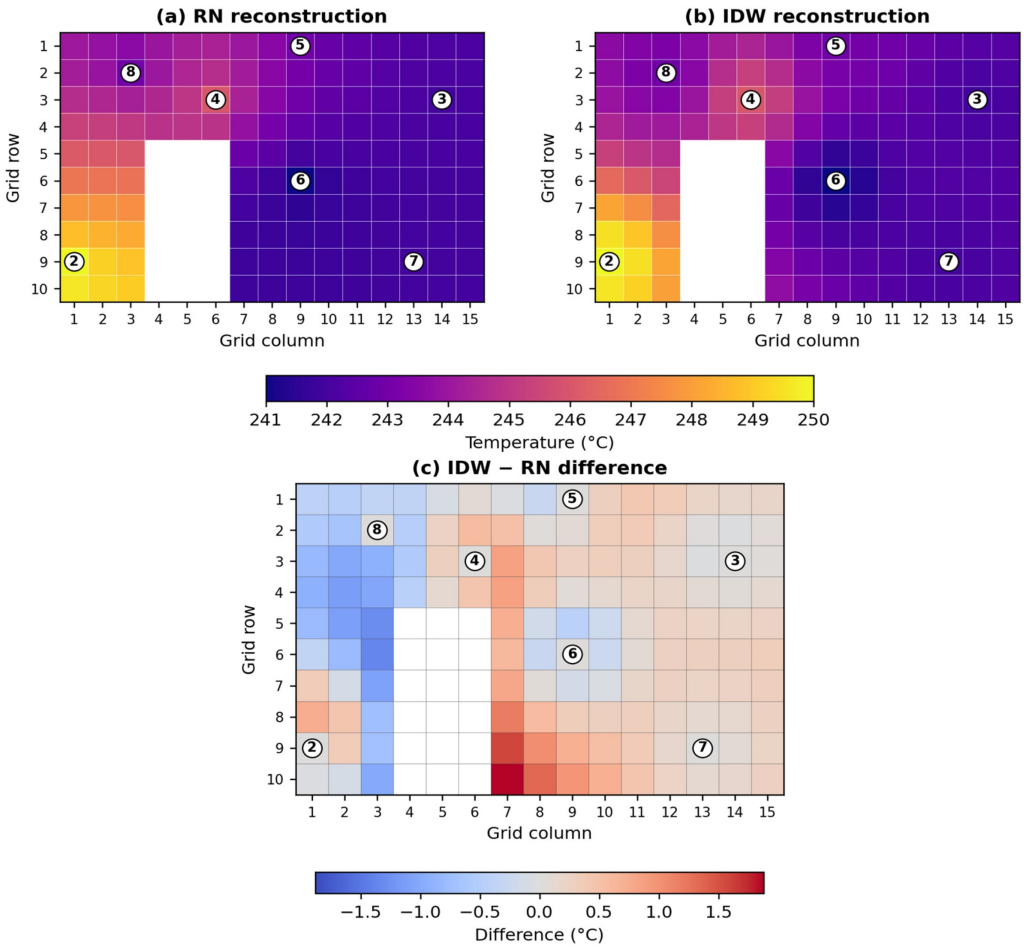


Figure 6. Comparison of RN and IDW reconstructions on the synthetic concave domain: (**a**) RN field; (**b**) IDW field; (**c**) cell-wise difference between IDW and RN. Numbered circles indicate the seven measurement points, and white cells indicate the numerically removed region.

3.5. Numerical Agreement of the Influence-Matrix Reconstruction

For identical geometry, sensor locations, initial values, and iteration count, the field calculated from the influence matrix agreed with the direct RN field to within rounding precision. The maximum cell-wise absolute difference remained below 10^{-12} °C. This is at least seven orders of magnitude smaller than the maximum update value of 0.00003 °C measured at iteration 500 and more than twelve orders of magnitude smaller than the nominal thermocouple accuracy of ±1.5 °C.

The numerical agreement demonstrates that the influence-matrix variant introduced no new approximation into the investigated linear model. The linear combination of the seven basis fields obtained from unit excitations reproduced the same finite Jacobi-iteration mapping that the direct RN repeated for every new measurement vector. The acceleration therefore caused no detectable loss of accuracy; the difference between the two variants appeared only at the rounding level resulting from the order of floating-point operations.

This finding distinguishes the reconstruction-model error from the numerical error of the acceleration. The RN deviations of 0.45–2.83 °C observed in leave-one-out validation arise from sparse measurement information and the assumptions of the harmonic model; the influence-matrix evaluation added no measurable error. With an unchanged W matrix, the accuracy of subsequent measurement states is therefore limited by the same factors as the direct RN solution.

3.6. Runtime, Acceleration, and Break-Even Point

Table 6 compares the runtimes of the direct RN, influence-matrix construction, and online matrix multiplication. Direct-solution time increased with the iteration count: 0.00336 s at 100 iterations, 0.00637 s at 200 iterations, and 0.01684 s at 500 iterations. Influence-matrix construction required 0.02277, 0.04547, and 0.11574 s, respectively, for the same settings. The small differences in RN runtime relative to Table 2 arose from separate repeated timing series and are of the same order as timing fluctuations in VBA runs lasting hundredths of a second. The preprocessing time was 6.78, 7.14, and 6.87 times that of one direct RN run, respectively, consistent with separate calculation of the seven basis fields for the seven sensors.

Table 6. Comparison of computation times for the RN and influence-matrix variant.

Iterations	RN (s)	Influence-Matrix Construction (s)	Online Evaluation (s)	Acceleration
100	0.00336	0.02277	0.00027	12.44×
200	0.00637	0.04547	0.00027	23.59×
500	0.01684	0.11574	0.00031	54.32×

By contrast, online evaluation time remained between 0.00027 and 0.00031 s and varied only slightly with the number of iterations used for the offline basis fields. This is because no iteration was performed in the online stage: in every case, the same seven-column influence matrix was multiplied by the current sensor vector. Acceleration relative to the direct RN therefore increased with the iteration count: it was 12.44-fold at 100 steps, 23.59-fold at 200 steps, and 54.32-fold at 500 steps.

For the final 500-iteration setting, one direct RN measurement state required 0.01684 s, whereas online influence-matrix evaluation required 0.00031 s. Owing to the one-time preprocessing cost of 0.11574 s, however, total processing of the first few states remained slower than the direct method. Using the rounded mean times, the total times at seven states were practically identical: 0.11788 s for repeated RN and 0.11791 s for the influence-matrix route. At eight states, the influence-matrix total was 0.11822 s, compared with 0.13472 s for the direct RN; the break-even number of evaluations was therefore $N = 8$. Table 7 summarizes the cumulative runtimes.

Table 7. Cumulative runtime and time saving for the 500-iteration setting. A positive time saving indicates an advantage of the influence-matrix procedure.

Number of States, N	Repeated RN (s)	Influence Matrix, Total (s)	Time Saving (s)
1	0.01684	0.11605	−0.09921
5	0.08420	0.11729	−0.03309
7	0.11788	0.11791	−0.00003
8	0.13472	0.11822	+0.01650
10	0.16840	0.11884	+0.04956
100	1.68400	0.14674	+1.53726

At ten measurement states, the total time saving was 0.04956 s; at one hundred states, it was 1.53726 s. In the latter case, influence-matrix processing including preprocessing was completed in 0.14674 s, compared with 1.68400 s for repeated RN, corresponding to an 11.48-fold acceleration of the complete process and a time saving of approximately 91.3%. At larger numbers of states, the specific effect of one-time preprocessing decreases further, and the aggregate acceleration gradually approaches the 54.32-fold ratio of the online stage.

Figure 7 shows the intersection of the two cumulative time curves over the first 20 states. The direct RN time increases steeply and linearly with the number of states, while the

influence-matrix curve begins at a higher value but rises only slightly because of the low cost of online evaluation. From the eighth state onward, the accelerated solution is more favorable not only per state but also in aggregate, including preprocessing. This break-even point is valid only for unchanged geometry, sensor locations, model parameters, and iteration settings; rebuilding W starts a new preprocessing cycle.

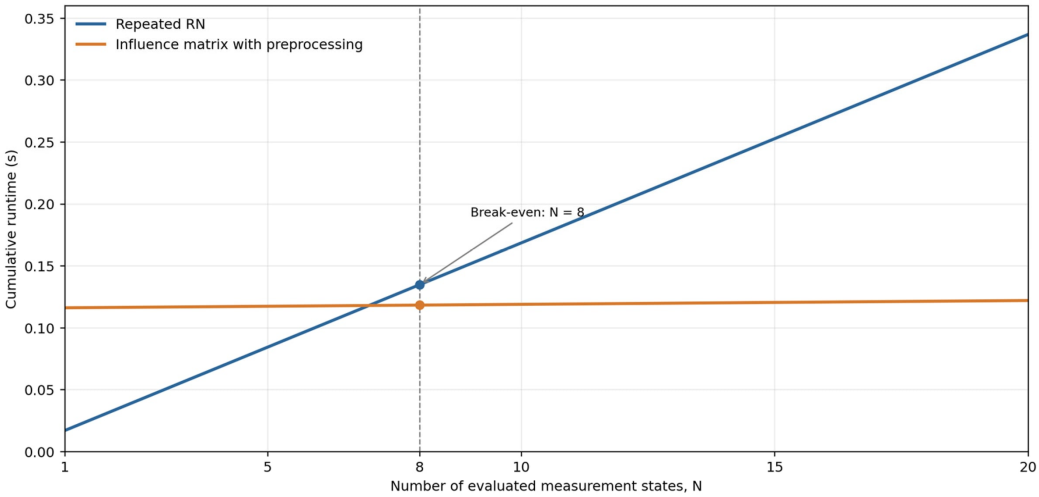


Figure 7. Cumulative runtime of repeated RN evaluation and the influence-matrix procedure including preprocessing for the 500-iteration setting. The influence-matrix variant becomes faster overall from the eighth evaluated measurement state onward.

4. Discussion

4.1. Interpretation of Resistor-Network Reconstruction

The results show that resistor-network reconstruction produced a smooth temperature field between the seven fixed measurements while conforming to the connectivity of the computational domain. No value occurred outside the measured range of 241–250 °C, which is a direct consequence of the maximum principle for the discrete harmonic solution. This is favorable when few measurement points are available because the method does not create over- or undershoot unsupported by sensor data. Nevertheless, the resulting field cannot be regarded as a unique determination of the complete thermal state of the PCB. The Laplace condition imposes local smoothness on unmeasured cells but does not separately represent convection, radiation, internal heat sources, or the detailed thermal-conduction properties of the material structure.

The method can therefore be interpreted as a regularized interpolation that reconstructs missing spatial information by assuming equilibration among neighboring cells. Unknown-cell values are determined from the values of connected cells; thus, the reconstruction does not fit a preselected global surface between measurement points but satisfies local equilibrium defined on the grid. This agrees with the mathematical interpretation of interpolation based on the graph Laplacian [11,13,14]. The resistor-network analogy provides physical intuitiveness, but it does not imply that uniform grid edges accurately represent identical thermal conduction at every location and in every direction of the actual PCB.

The smoothness condition also defines a fundamental limitation of the method. A local extreme that is not detected by any nearby sensor cannot be recovered in a harmonic field. This was also evident when sensor 4 was omitted: the RN reconstructed the local maximum of 246 °C at a value 2.83 °C lower. The 0.00003 °C update reported in Table 2 pertains to the seven-sensor baseline and does not establish the remaining numerical error

in this omitted-sensor case. The observed deviation is consistent with the limited local information available to a harmonic reconstruction.

In this study, the 10 × 15 cell resolution provided a simple, computationally small representation of the PCB surface. Refining the grid could represent the outline, cutouts, and sensor locations in greater detail, but it would not by itself increase the available measurement information. The same seven temperatures would be distributed over a larger number of cells; consequently, an apparent increase in spatial detail would not equal an increase in the effective resolution of the reconstruction. Grid resolution should therefore be selected by jointly considering geometric description, sensor density, and computational cost.

4.2. Implications of Validation and Sensor Layout

The leave-one-out results indicated a moderate RN advantage that was not identical across all error metrics. The mean absolute error was 10.04% lower and the maximum absolute error 8.43% lower than those of IDW with $p = 2$, whereas the RMSE difference was only 0.010 °C, or approximately 0.54%. On the basis of five validation cases, a general accuracy superiority of the RN cannot be claimed. For the comparison with $p = 2$, the narrower conclusion is that, for the investigated sensor layout and measurement state, the RN produced a smaller absolute deviation at most omitted points, while the root mean square errors remained essentially identical because of the two larger errors. The extended IDW comparison reinforces this limitation: RN retained the lowest MAE, whereas IDW with $p = 1$ achieved the lowest RMSE among the compared settings.

The spatial pattern of pointwise errors provides more information than aggregate metrics alone. At sensor 4, both methods produced a value lower than the measurement, indicating that the omitted value of 246 °C was locally elevated relative to its surroundings. For sensor 8, both methods produced values above the reference of 243 °C, and IDW was more favorable. The identical error signs indicate that both reconstructions were constrained by the same sparse measurement geometry. Method selection affected the magnitude of the deviation but did not eliminate the local uncertainty caused by missing information.

Retaining the sensors that recorded the global minimum and maximum was methodologically necessary to ensure that every investigated case remained an interpolation within the observed temperature range. Consequently, the validation does not show how the procedure would behave if the hottest or coldest point were lost. If the sensor recording the maximum of 250 °C were omitted, the upper bound of the reconstructed harmonic field would be determined by the remaining measurements because of the maximum principle; recovery of the original peak would not be expected without additional physical or statistical information. The results therefore concern the reconstructability of internal measurement points, not prediction of the extrema of the complete measurement range.

The nominal thermocouple accuracy of ±1.5 °C introduces an additional interpretive limitation. The omission error is not solely a reconstruction error because the reference value itself is affected by measurement uncertainty, and the sensor attachment, geometry, and thermal capacitance may alter the measured transient response [4]. Nominal accuracy therefore cannot be used as a simple acceptance threshold. Without repeated measurements, an independent reference, and an uncertainty budget, a deviation below 1.5 °C does not prove that the field is correct, while a larger deviation cannot be attributed exclusively to interpolation.

Thermocouple type, wire and junction dimensions, and attachment conditions should therefore be considered when interpreting the measurements [4,32]. Moreau et al. [32] compared high-temperature solder, polyimide and aluminum tapes, and thermally conductive adhesives during PCB reflow profiling. Their experiments showed that larger solder

volumes increased local thermal mass and slowed the heating and cooling response, while attachment failures interrupted measurements. These findings provide context for the uncertainty of the reconstruction inputs; they do not establish the accuracy of the present industrial dataset or a universally superior attachment method.

The influence of sensor locations appeared in the results of both the RN and IDW. The literature on sparse sensing indicates that the information content of measurement points can be at least as important as the selected reconstruction algorithm [26,27]. In the present procedure, the influence matrix may also provide a direct basis for this analysis: its columns show the spatial response generated by a unit change at each sensor. Future sensor-placement studies could therefore be based not only on geometric distance, but also on the distinguishability of influence fields, omission errors, or matrix conditioning.

4.3. Role of Domain Shape and Topology

Comparison of the rectangular and synthetic concave domains showed that the geometric obstacle is represented differently by the two interpolation methods. Introducing the concave mask increased the full-field RMSE between IDW and RN by 13.24% and the maximum cell-wise difference by 10.64%. The increase does not in itself demonstrate an error in either method, but it makes visible their different definitions of spatial connection. The RN propagates sensor influence along cell connections within the domain, whereas the applied IDW weights values according to straight-line Euclidean distance.

The practical importance of this difference may increase for boards with irregular outlines or cutouts. In the RN, a hole, slot, or removed region can be represented by eliminating the corresponding grid connections; consequently, the model transmits no direct neighborhood influence across the obstacle. IDW could account for the same feature only by using a modified distance metric, such as a shortest path within the domain, or by applying separate obstacle handling. Similar differences between Euclidean-distance and graph-connectivity methods have been observed in interpolation of network data [11].

The synthetic cutout, however, served only to demonstrate the topological mechanism. No dense, independent reference field was available; therefore, the differences in Table 5 cannot be interpreted as accuracy metrics. On an actual PCB, internal layers, copper traces, plated through-holes, and components may create thermal-conduction paths that are not represented by a simple two-dimensional mask. A geometric gap therefore does not necessarily imply complete thermal separation, and the correct graph must be adapted to the actual structure.

An advantage of the resistor-network formulation is that this extension can be implemented without changing the structure of the model. Direction- and location-dependent weights can replace uniform edge conductances, thereby approximating the effects of copper coverage, layer stack-up, or anisotropic thermal conduction. A weighted graph would, however, require additional material or calibration information. The simple interpolation with little prior data would then gradually become a more detailed physical model; the necessary complexity should therefore be matched to the accuracy requirements of the application.

4.4. Practical Value of Influence-Matrix Acceleration

The maximum difference below 10^{-12} °C between the direct RN and RN-IM confirmed that influence-matrix evaluation did not degrade reconstruction accuracy in the investigated linear setting. The matrix stores the basis field associated with each sensor; hence, the effect of a new temperature vector can be generated by linear combination. The RN deviations with absolute values of 0.45–2.83 °C observed in leave-one-out validation thus arose from sparse measurement data and model assumptions, not from the acceleration. This distinction is

important because simplifying online computation is acceptable only if it does not introduce an additional approximation separate from model error.

For the 500-iteration setting, the online matrix–vector product was 54.32 times faster than one direct RN run. The one-time preprocessing cost, however, was equivalent to approximately seven direct reconstructions; consequently, the complete process became faster only from the eighth measurement state. This break-even point is readily interpreted from the seven basis fields required for the seven sensors. Constructing the influence matrix has no computational justification when only one state is processed, but preprocessing is rapidly amortized in repeated evaluations.

In a reflow process, temperature vectors are generally available at consecutive time instants for the same PCB geometry and sensor layout. In such a setting, eight states constitute a low threshold: a complete thermal profile or several repeated manufacturing cycles may contain orders of magnitude more evaluations. At 100 states, the measured acceleration of the complete process was 11.48-fold and the time saving was 91.3%, even when preprocessing was included. This result indicates that the RN-IM is primarily advantageous not for a single field calculation but for repeated online application of the same model.

Absolute runtimes depend on the computer, spreadsheet and VBA execution, and timing method; therefore, they cannot be transferred unchanged to another environment. The observed structural difference is more general: the direct procedure repeats the iteration for every state, whereas the online stage of the RN-IM performs only one fixed-size matrix multiplication. For a larger grid or more sensors, preprocessing time, storage demand, and the break-even point would also change. Practical deployment should therefore be benchmarked again on the target hardware, using the actual amount of data and accounting for the complete data-processing chain.

The acceleration requires the model to remain unchanged. If the PCB shape, set of active cells, sensor locations, cell-connection weights, or numerical settings change, the influence matrix must be recalculated. Changes in sensor values alone do not require new preprocessing because their linear mapping is precisely the operation performed by the fixed W matrix. This separation is well suited to a manufacturing task in which the same product type and measurement layout are evaluated over many cycles, but it is less advantageous when the geometry or sensor layout changes frequently.

4.5. Position of the Method Among Reconstruction Approaches

The RN/RN-IM approach lies between simple geometric interpolation and detailed physics-based or data-driven reconstruction. Finite-element and analytical reflow models can describe several heat-transfer mechanisms, but they require geometric, material, and boundary-condition data and often calibration [1–3]. POD-based, reduced-order, and learning-based methods can provide rapid online evaluation, but their performance depends on representative prior fields or training data [15–19,23,24,26]. The RN uses less prior information: graph connectivity and current sensor values are sufficient to determine the harmonic field.

IDW, point-interpolation, and radial-basis-function methods can also be applied when few measurement points are available [10,20–22]. Their advantages are simplicity and direct handling of irregular sensor locations, but internal domain connectivity appears only if it is incorporated separately into the distance measure or basis functions. In this comparison, the main added value of the RN is not the small accuracy difference measured for the present dataset, but the explicit and reproducible treatment of topology. The associated cost is the homogeneous smoothness assumption and the fact that detailed thermal-physics effects can be incorporated only through additional weights or model extensions.

Validation evidence also differs between these approaches. Reflow recipe studies [6,7] assess process settings and temperature or quality predictions. The sparse-field studies of Ye et al. [8] and Wang et al. [18] use analytical or CFD-based cases, whereas PEGNN [30] includes distribution-shift tests and the graph-prior study [31] varies sensor counts and noise. Here, measurement-based evaluation covers five omitted sensor values from one state; RN–IM agreement with RN is a separate numerical check. These tests provide different levels and types of evidence for deployment.

Computational comparisons must separate preparation from repeated evaluation. POD requires prior fields and mode extraction, and neural approaches require training. Graph-prior assimilation also solves a regularized coefficient or latent-variable problem for the observations. RN-IM requires one basis calculation per sensor and then uses a matrix–vector product for each new state. Fixed IDW weights can also be precomputed. The 54.32-fold speed ratio reported here compares RN-IM only with the implemented 500-step Jacobi RN solver; it is not a runtime ranking against other reconstruction methods.

Table 8 summarizes study-specific evidence and computational stages; it is a qualitative comparison, not a benchmark on common data or hardware. No method family can be considered preferable for every application. If a reliable material model and accurate boundary conditions are available, detailed physical simulation may provide more causal information. With a large, representative database of fields, POD or learning-based methods may exploit complex spatial patterns. The RN/RN-IM offers an advantage in the narrower situation where few measured data are available, domain topology is known, no detailed calibrated thermal model exists, and the same measurement geometry must be evaluated repeatedly. Its contribution is the evaluation of this combination under an existing industrial measurement arrangement, with explicit connectivity and preprocessing amortization. Neither harmonic interpolation nor linear precomputation is claimed as a new mathematical principle.

Table 8. Assumptions, validation evidence, and computational stages of selected reconstruction approaches.

Approach	Information and Assumptions	Validation or Evidence	Offline Work	Online Evaluation
Reflow thermal models [1–3,5]	Geometry, material properties and thermal boundary conditions	Model-specific simulation and experimental checks [3]	Build and calibrate the physical model	Solve the thermal model
IDW [10]	Sensor positions, temperatures and a distance exponent; no connectivity constraint	Here: five omitted sensors, with $p = 1$, 2 and 3	Distance weights can be precomputed	Weighted sums
RN (this study)	Uniform harmonic graph, domain mask and fixed sensor values	Five omitted sensors; no independent full-field reference	Construct the grid graph	500 Jacobi iterations
RN-IM (this study)	The same RN operator; fixed geometry and sensor layout	Numerical agreement with RN; inherits its measurement limitations	One basis solve per sensor	Matrix–vector product
POD methods [8,18]	Prior field samples and a low-dimensional representation	Analytical or CFD cases; sensor-layout comparisons	Generate fields and extract modes	Estimate coefficients and assemble the field
PEGNN [30]	Graph, physical operators and training data	Neural baselines and distribution-shift tests	Train the graph network	Network inference
Graph-prior POD/Graph AE [31]	CFD mesh topology and a reduced representation	Data-center cases; sensor-count and noise tests	Construct the graph and representation	Regularized coefficient or latent inversion

4.6. Limitations and Directions for Further Development

The principal limitation of this study is that it was based on seven temperature values from a single selected measurement state of one PCB. Leave-one-out validation at five internal points is suitable for internal verification of the computational procedure and comparison with IDW under identical conditions, but it is insufficient for statistical generalization. The data do not allow analysis of variability among manufacturing cycles, the effect of different board types, sensor repeatability, or changes in spatial patterns over a complete reflow profile. The reported error metrics are therefore case-study results, not general performance bounds. The IDW sensitivity check covers only $p = 1$, 2, and 3. A wider parameter search and comparisons with other interpolants, such as radial basis functions, were not performed and would be needed for a broader benchmark.

A further limitation is the absence of an independent reference temperature at unmeasured cells. Point omission validated the reconstruction only at sensor locations, not the correctness of the complete field. The RN–IDW difference on the concave domain quantifies distinct behavior of the methods but does not determine which field more closely approximates the actual temperature. Denser thermocouple measurements, appropriately corrected infrared thermography, or a validated detailed thermal simulation could provide an independent reference.

The two-dimensional, quasi-steady-state, homogeneous model did not include through-thickness temperature differences, temporal heat storage, the varying thermal load of oven zones, the shielding and thermal-capacitance effects of components, or the spatially varying conductivity of copper layers. The result therefore cannot be used directly for complete physical prediction of the soldering process. The purpose of the present approach was to reconstruct the surface-temperature field between measurement points at a selected instant. A transient extension may require temporal regularization or a dynamic model describing heat storage in addition to independent reconstruction of consecutive states.

In the next stage of investigation, the reconstruction should be repeated for several PCBs, manufacturing cycles, and time instants over the complete thermal profile. Systematic variation in sensor number and location would allow the spatial causes of errors to be separated from the effect of sensor density. A weighted resistor network could be used to investigate location- or direction-dependent thermal conduction, while the influence matrix could support sensor-sensitivity and uncertainty-propagation analyses. Sensor-placement optimization could be coupled with the QR-based or physics-based criteria used in the literature [26,27].

Further development of the numerical solution is also warranted for larger grids. In the present small problem, 500-step Jacobi iteration provided adequate numerical accuracy and short runtime, but convergence may deteriorate with network size. A residual-based stopping criterion, direct solution of the sparse linear system, or a faster iterative method could reduce offline computational cost. These changes would not alter the fundamental RN-IM principle: as long as the reconstruction remains a linear function of the fixed sensor values, the precomputed mapping can still be used for repeated online evaluation.

Overall, the results support the RN/RN-IM as a transparent reconstruction solution with low data requirements under the investigated conditions. In the leave-one-out comparison, the RN produced moderately smaller MAE and maximum error than IDW, and the topological example demonstrated the effect of explicitly treating cell connectivity. The influence matrix implemented the same numerical mapping at substantially lower online cost. Demonstrating practical applicability will nevertheless require more measurement states, an independent full-field reference, and a weighted model that better approximates the actual material structure of the PCB.

5. Conclusions

This study aimed to develop a method requiring few measurement data with which the surface-temperature distribution of a printed circuit board can be reconstructed at a selected reflow instant. The investigated domain of approximately 10 × 15 cm was represented by a 10 × 15 grid comprising 150 cells. Measured values from seven thermocouples acted as internal Dirichlet conditions, while the external and internal boundaries were reflecting. The resistor-network (RN) model determined the temperatures of unmeasured cells from the discrete Laplace equation. The method does not replace thermal simulation of the complete reflow process; it reconstructs a two-dimensional, quasi-steady-state temperature field between sparse point measurements.

The numerical behavior of the Jacobi iteration could be tracked clearly on the investigated grid. The maximum cell-wise change between two consecutive fields was 0.90921 °C at 100 iterations, 0.06913 °C at 200 iterations, and 0.00003 °C at 500 iterations. The field obtained with 500 iterations remained within the measured range of 241–250 °C in every active cell; thus, the computation did not create artificial over- or undershoot. This result supports the stability of the applied numerical setting, but it does not by itself validate the physical correctness of the complete unmeasured temperature field.

In leave-one-out validation at five internal measurement points, the RN produced a mean absolute error of 1.390 °C, an RMSE of 1.785 °C, and a maximum absolute error of 2.826 °C. Applied to the same data with $p = 2$, IDW yielded an MAE of 1.545 °C, an RMSE of 1.795 °C, and a maximum error of 3.086 °C. The RN achieved a smaller absolute deviation in four of five omission cases, and its MAE was 10.04% lower. The RMSE difference of only 0.010 °C shows that RN and IDW with $p = 2$ performed similarly for this small sample. With $p = 1$, IDW achieved a lower RMSE of 1.748 °C; RN retained a lower MAE than all three IDW settings. For each method, three errors remained within the nominal accuracy of ±1.5 °C for K-type, accuracy-class-1 thermocouples, while two exceeded it. The observed advantage therefore applies to the investigated measurement layout and should not be interpreted as a general statistical ranking.

The synthetic concave domain illustrated the principal structural characteristic of the RN: temperature influence propagates through the connectivity network of active cells; consequently, cutouts and obstacles are incorporated directly into the reconstruction. The RMSE between the complete IDW and RN fields increased from 0.4797 °C on the rectangular domain to 0.5432 °C on the concave domain, while the maximum difference increased from 1.6981 to 1.8788 °C. These are not measurement errors because no independent reference was available in nonsensor cells; rather, they quantify how explicit treatment of domain topology measurably modifies the reconstructed field. This advantage may be particularly relevant to geometries containing cutouts, openings, or separated subregions.

The influence-matrix RN-IM variant divided the same linear reconstruction into one-time offline preprocessing and repeated online evaluation. The maximum cell-wise difference between the field calculated using the influence matrix formed from seven unit excitations and the direct RN result remained below 10^{-12} °C; therefore, the acceleration caused no detectable loss of accuracy in the investigated model. For the 500-iteration setting, online matrix–vector multiplication required 0.00031 s, compared with 0.01684 s for the direct RN, corresponding to a 54.32-fold per-state acceleration. Preprocessing, which required 0.11574 s, was amortized at the eighth measurement state. When 100 states were processed together, the complete acceleration including preprocessing was 11.48-fold, and the time saving was approximately 91.3%.

Together, the RN and RN-IM form a transparent reconstruction framework that does not require a database of previous complete temperature fields or a detailed, calibrated material model. The direct RN requires little preparation and is therefore appropriate when

few states are to be evaluated. The RN-IM is advantageous when many time instants, manufacturing cycles, or parameter variants must be processed for the same PCB geometry and sensor layout. In this setting, the fixed influence matrix enables rapid, deterministic online reconstruction. The matrix must, however, be recalculated if the domain shape, connectivity of active cells, sensor locations, cell-connection weights, or numerical settings change.

The results clearly separate reconstruction accuracy from the effect of computational acceleration. RN leave-one-out errors characterize how well the harmonic model constructed from sparse sensor data, homogeneous cell connections, and the selected boundary conditions can reconstruct an omitted measured value. By contrast, the numerical agreement of the RN-IM does not improve the accuracy of the physical model; it verifies that the same linear mapping can be precomputed and subsequently applied without iteration. The influence matrix therefore neither compensates for an unfavorable sensor layout, missing local information, or model simplifications, nor alters them. From a practical perspective, precisely this identity makes the procedure interpretable: validation results obtained with the direct RN also apply to online RN-IM evaluation for the same fixed model.

Industrial implementation of the RN-IM should therefore be subject to two consecutive checks. First, the RN reconstruction error must be shown to be acceptable for the purpose of the task and for the particular product and sensor layout, preferably using several measurement cycles and an independent reference. Only then is construction and repeated use of the influence matrix justified. In the online stage, reading the current vector of seven sensor values and performing the matrix–vector product are sufficient, but the geometry, sensor locations, and applied numerical model must be monitored for change. Under these conditions, the method may support rapid spatial reconstruction of thermal profiles, comparison of repeated manufacturing cycles, or generation of visualizations that provide more information on the spatial structure of the temperature distribution than a small number of point measurements. The reconstructed field, however, is meaningful only within the validity range of the validated model and does not replace the direct measurements required for process qualification.

Interpretation of the results is governed by the limitations of the study. The computation used seven sensor values from one measurement state of one PCB; validation covered five internal points, and no independent high-spatial-resolution reference field was available. The model is homogeneous, two-dimensional, and quasi-steady-state; therefore, it does not describe through-thickness temperature differences, transient heat storage, location-dependent effects of components and copper layers, or the varying thermal load of the reflow oven. Further studies should include several PCBs, multiple manufacturing cycles, and several time instants over complete thermal profiles. A denser sensor layout or corrected infrared reference could be used to validate the complete field, while weighted cell connections could represent location- and direction-dependent thermal conduction. Sensor-placement optimization, propagation of measurement uncertainty, and faster solvers suitable for larger grids are also important directions for further development.

Under the investigated conditions, RN provided lower MAE than IDW at $p = 1$, 2, and 3, while IDW with $p = 1$ gave a lower RMSE. RN explicitly represented domain connectivity, and RN-IM enabled substantially faster repeated evaluation of the same reconstruction. The two procedures may thus be useful particularly in industrial tasks where few sensors are available, domain connectivity is known, and many measurement states must be processed rapidly under an unchanged configuration.

Author Contributions: Conceptualization, Á.G.M. and Á.M.; methodology, Á.G.M.; software, Á.G.M.; validation, Á.G.M.; formal analysis, Á.G.M.; investigation, Á.G.M., R.R.B. and A.T.; resources, Á.G.M. and Á.M.; data curation, Á.G.M.; writing—original draft preparation, R.R.B.; writing—review and

editing, R.R.B. and A.T.; visualization, Á.G.M. and R.R.B.; supervision, Á.M. and A.T.; project administration, Á.M. and A.T. All authors have read and agreed to the published version of the manuscript.

Funding: This research received no external funding.

Data Availability Statement: The original contributions presented in this study are included in the article. Further inquiries can be directed to the corresponding author. The seven temperature values and their grid coordinates for the measurement state analyzed in this study are provided in Table 1. The numerical temperature fields reconstructed using the RN and IDW methods are reported in Tables A1 and A2, respectively. A complete time-resolved thermal profile is not available.

Conflicts of Interest: The authors declare no conflicts of interest.

Abbreviations

The following abbreviations are used in this manuscript:

Gappy POD	Gappy proper orthogonal decomposition
IDW	Inverse distance weighting
MAE	Mean absolute error
MBE	Mean bias error
PCB	Printed circuit board
POD	Proper orthogonal decomposition
QR	Matrix factorization into an orthogonal matrix Q and an upper triangular matrix R
RMSE	Root mean square error
RN	Resistor network
RN-IM	Resistor-network influence-matrix method
VBA	Visual Basic for Applications

Appendix A

Appendix A.1. Numerical Values of the RN Reconstruction

Table A1 contains the RN field obtained after 500 Jacobi iterations. Row indices increase from top to bottom and column indices from left to right; values are given in °C. Bold cells with heavy borders indicate the locations of the seven directly measured temperatures.

Table A1. Numerical values of the 10 × 15 surface-temperature field reconstructed using the RN method (°C).

Row/ Column	1	2	3	4	5	6	7	8	9	10	11	12	13	14	15
1	243.80	243.67	243.52	243.90	244.24	244.36	244.06	243.58	**243.00**	242.83	242.64	242.47	242.33	242.22	242.18
2	243.93	243.69	**243.00**	243.94	244.46	244.77	244.25	243.67	243.16	242.84	242.62	242.44	242.29	242.16	242.14
3	244.29	244.18	244.04	244.39	244.91	**246.00**	244.52	243.68	243.12	242.77	242.55	242.38	242.22	**242.00**	242.09
4	244.76	244.69	244.61	244.66	244.77	244.83	244.14	243.43	242.85	242.58	242.43	242.31	242.21	242.12	242.11
5	245.30	245.20	245.04	244.88	244.70	244.39	243.79	243.04	242.29	242.26	242.27	242.24	242.19	242.15	242.13
6	245.95	245.76	245.47	245.13	244.75	244.26	243.59	242.64	**241.00**	241.90	242.14	242.19	242.17	242.15	242.13
7	246.80	246.43	245.94	245.42	244.89	244.32	243.67	242.94	242.21	242.20	242.22	242.20	242.16	242.14	242.13
8	248.01	247.22	246.44	245.73	245.08	244.45	243.83	243.22	242.72	242.48	242.33	242.22	242.12	242.11	242.11
9	**250.00**	248.02	246.86	245.98	245.24	244.57	243.96	243.41	242.96	242.65	242.42	242.23	**242.00**	242.08	242.09
10	249.00	248.00	246.99	246.10	245.33	244.65	244.04	243.51	243.07	242.73	242.48	242.28	242.13	242.10	242.10

Cell background colors indicate temperature, with blue representing lower temperatures and red representing higher temperatures. Bold values enclosed by thick black borders identify the seven directly measured temperatures; the remaining values are reconstructed.

Appendix A.2. Numerical Values of the IDW Reconstruction

Table A2 contains the IDW field generated from the same seven measured values using $p = 2$. Row and column indices follow the definitions used in Table A1; values are given in °C. Bold cells with heavy borders indicate the locations of the seven directly measured temperatures.

Table A2. Numerical values of the 10 × 15 surface-temperature field reconstructed using IDW interpolation (°C).

Row/ Column	1	2	3	4	5	6	7	8	9	10	11	12	13	14	15
1	243.63	243.36	243.25	243.58	244.19	244.42	243.98	243.26	**243.00**	243.05	242.97	242.73	242.48	242.34	242.34
2	243.64	243.24	**243.00**	243.50	244.74	245.32	244.69	243.60	243.15	243.05	242.87	242.56	242.25	242.11	242.16
3	243.90	243.51	243.37	243.97	245.28	**246.00**	245.22	243.91	243.21	242.92	242.70	242.43	242.13	**242.00**	242.09
4	244.45	244.14	244.06	244.40	245.03	245.35	244.65	243.42	242.67	242.48	242.46	242.37	242.19	242.09	242.15
5	245.33	244.97	244.70	244.60	244.60	244.38	243.54	242.27	241.59	241.81	242.16	242.30	242.28	242.24	242.26
6	246.58	246.10	245.47	244.91	244.43	243.81	242.82	241.59	**241.00**	241.42	241.97	242.22	242.28	242.29	242.32
7	248.14	247.56	246.52	245.46	244.56	243.71	242.76	241.85	241.42	241.65	242.02	242.18	242.20	242.24	242.30
8	249.49	248.92	247.58	246.11	244.89	243.90	243.05	242.39	242.06	242.07	242.15	242.12	242.07	242.13	242.24
9	**250.00**	249.50	248.15	246.58	245.24	244.20	243.41	242.84	242.51	242.35	242.23	242.08	**242.00**	242.07	242.21
10	249.61	249.17	248.06	246.68	245.44	244.45	243.71	243.17	242.80	242.54	242.33	242.15	242.07	242.13	242.25

Cell background colors indicate temperature, with blue representing lower temperatures and red representing higher temperatures. Bold values enclosed by thick black borders identify the seven directly measured temperatures; the remaining values are reconstructed.

References

1. Whalley, D.C. A simplified reflow soldering process model. *J. Mater. Process. Technol.* **2004**, *150*, 134–144. [CrossRef]
2. Van Steenberge, N.; Limaye, P.; Willems, G.; Vandevelde, B.; Schildermans, I. Analytical and finite element models of the thermal behavior for lead-free soldering processes in electronic assembly. *Microelectron. Reliab.* **2007**, *47*, 215–222. [CrossRef]
3. Esfandyari, A.; Bachy, B.; Raithel, S.; Syed-Khaja, A.; Franke, J. Simulation, optimization and experimental verification of the over-pressure reflow soldering process. *Procedia CIRP* **2017**, *62*, 565–570. [CrossRef]
4. Straubinger, D.; Illés, B.; Busek, D.; Codreanu, N.; Géczy, A. Modelling of thermocouple geometry variations for improved heat transfer monitoring in smart electronic manufacturing environment. *Case Stud. Therm. Eng.* **2022**, *33*, 102001. [CrossRef]
5. Ran, L.; Chen, D.; Chen, C.; Gong, Y. Optimization Method for Hot Air Reflow Soldering Process Based on Robust Design. *Processes* **2023**, *11*, 2716. [CrossRef]
6. Zhang, Z.; Li, Y.; Yoon, S.W.; Won, D. Stage-based neural network for reflow profile prediction and reflow recipe optimization for quality and energy-saving. *Int. J. Adv. Manuf. Technol.* **2025**, *137*, 1745–1757. [CrossRef]
7. Li, Y.; Zhang, Z.; Won, D.; Yoon, S.W. Soldering reflow process optimization based on simulation. *Int. J. Adv. Manuf. Technol.* **2025**, *136*, 3163–3176. [CrossRef]
8. Ye, Y.; Ai, Q.; Zhang, X.; Liu, M.; Shuai, Y. A rapid reconstruction strategy of full-domain temperature field based on discrete measurement points for electronics thermal management. *Adv. Eng. Softw.* **2025**, *206*, 103935. [CrossRef]
9. Yuan, Q.; Yao, P.; Zhao, W.; Zhang, B. Optimization of sparse sensor layouts and data-driven reconstruction methods for steady-state and transient thermal field inverse problems. *Sensors* **2025**, *25*, 4984. [CrossRef] [PubMed]
10. Shepard, D. A two-dimensional interpolation function for irregularly-spaced data. In Proceedings of the 23rd ACM National Conference, Las Vegas, NV, USA, 27–29 August 1968; pp. 517–524. [CrossRef]
11. Jara-Arriagada, C.; Stoianov, I. Spatial interpolation of pressure transient metrics for improved water distribution network asset management. *Water Resour. Res.* **2025**, *61*, e2024WR039742. [CrossRef]
12. Zhu, X.; Ghahramani, Z.; Lafferty, J. Semi-Supervised Learning Using Gaussian Fields and Harmonic Functions. In Proceedings of the 20th International Conference on Machine Learning (ICML), Washington, DC, USA, 21–24 August 2003; pp. 912–919. Available online: https://cdn.aaai.org/ICML/2003/ICML03-118.pdf (accessed on 27 September 2026).
13. Narang, S.K.; Gadde, A.; Ortega, A. Signal processing techniques for interpolation in graph structured data. In Proceedings of the 2013 IEEE International Conference on Acoustics, Speech and Signal Processing, Vancouver, BC, Canada, 26–31 May 2013; pp. 5445–5449. [CrossRef]
14. Shi, Z.; Osher, S.; Zhu, W. Weighted nonlocal Laplacian on interpolation from sparse data. *J. Sci. Comput.* **2017**, *73*, 1164–1177. [CrossRef]
15. Everson, R.; Sirovich, L. Karhunen–Loève procedure for gappy data. *J. Opt. Soc. Am. A* **1995**, *12*, 1657–1664. [CrossRef]
16. Willcox, K. Unsteady flow sensing and estimation via the gappy proper orthogonal decomposition. *Comput. Fluids* **2006**, *35*, 208–226. [CrossRef]
17. Jiang, G.; Kang, M.; Cai, Z.; Wang, H.; Liu, Y.; Wang, W. Online reconstruction of 3D temperature field fused with POD-based reduced order approach and sparse sensor data. *Int. J. Therm. Sci.* **2022**, *175*, 107489. [CrossRef]
18. Wang, X.; Cao, Z.; Liu, Y.; Wang, F. Temperature reconstruction in data centers using gappy POD combined with genetic algorithm and optimization of sensor layout. *Energy Build.* **2025**, *326*, 115078. [CrossRef]
19. Nassiopoulos, A.; Bourquin, F. Fast three-dimensional temperature reconstruction. *Comput. Methods Appl. Mech. Eng.* **2010**, *199*, 3169–3178. [CrossRef]

20. Guo, Y.; Wang, K.; Leng, G.; Zhao, F.; Bao, H. Real-time temperature field reconstruction using a few measurement points and RPIM-AGQ6 interpolation. *Measurement* **2024**, *225*, 114041. [CrossRef]
21. Cao, L.; Abedin, S.; BiondiVaccariello, A.M.; Wu, R.; Cui, G.; Cao, C.; Wang, X. 2D temperature field reconstruction using optimized Gaussian radial basis function networks. *Measurement* **2024**, *237*, 115170. [CrossRef]
22. Zhou, X.; Dong, C.; Zhao, C.; Bai, X. Temperature-field reconstruction algorithm based on reflected sigmoidal radial basis function and QR decomposition. *Appl. Therm. Eng.* **2020**, *171*, 114987. [CrossRef]
23. Fukami, K.; Maulik, R.; Ramachandra, N.; Fukagata, K.; Taira, K. Global field reconstruction from sparse sensors with Voronoi tessellation-assisted deep learning. *Nat. Mach. Intell.* **2021**, *3*, 945–951. [CrossRef]
24. Santos, J.E.; Fox, Z.R.; Mohan, A.; O'Malley, D.; Viswanathan, H.; Lubbers, N. Development of the Senseiver for efficient field reconstruction from sparse observations. *Nat. Mach. Intell.* **2023**, *5*, 1317–1325. [CrossRef]
25. Sabathiel, S.; Sanchis-Alepuz, H.; Wilson, A.S.; Reynvaan, J.; Stipsitz, M. Neural network-based reconstruction of steady-state temperature systems with unknown material composition. *Sci. Rep.* **2024**, *14*, 22265. [CrossRef] [PubMed]
26. Manohar, K.; Brunton, B.W.; Kutz, J.N.; Brunton, S.L. Data-driven sparse sensor placement for reconstruction: Demonstrating the benefits of exploiting known patterns. *IEEE Control Syst. Mag.* **2018**, *38*, 63–86. [CrossRef]
27. Liu, X.; Yao, W.; Peng, W.; Fu, Z.; Xiang, Z.; Chen, X. A physics-driven sensor placement optimization methodology for temperature field reconstruction. *Appl. Therm. Eng.* **2024**, *257*, 124476. [CrossRef]
28. Peter, P.; Hoffmann, S.; Nedwed, F.; Hoeltgen, L.; Weickert, J. Evaluating the true potential of diffusion-based inpainting in a compression context. *Signal Process. Image Commun.* **2016**, *46*, 40–53. [CrossRef]
29. Jumakulyyev, I.; Schultz, T. Combining Image Space and q-Space PDEs for Lossless Compression of Diffusion MR Images. *J. Math. Imaging Vis.* **2023**, *65*, 644–656. [CrossRef]
30. Li, Q.; Li, X.; Chen, X.; Yao, W. PEGNN: A physics embedded graph neural network for out-of-distribution temperature field reconstruction. *Int. J. Therm. Sci.* **2025**, *207*, 109393. [CrossRef]
31. Su, L.; Guo, Y.; Mo, X.; Zhang, L. Structure-aware robust data assimilation for data center temperature field reconstruction subject to sparse observations. *Appl. Therm. Eng.* **2026**, *304*, 132702. [CrossRef]
32. Moreau, M.; Anslem, M.; Brunhuber, A.; Shea, C.; Dworak, D. Thermocouple Tactics: A Comparative Study of Attachment Methods. *Glob. SMT Packag.* **2025**, *26*, 621–628. Available online: https://kicthermal.com/wp-content/uploads/2025/03/thermocouple-tactics-study.pdf (accessed on 24 October 2026). [CrossRef]

Disclaimer/Publisher's Note: The statements, opinions and data contained in all publications are solely those of the individual author(s) and contributor(s) and not of MDPI and/or the editor(s). MDPI and/or the editor(s) disclaim responsibility for any injury to people or property resulting from any ideas, methods, instructions or products referred to in the content.